

# Amplifying Sensing Capabilities: Combining Plasmonic Resonances and Fresnel Reflections through Multivariate Analysis

Jaione Etxebarria-Elezgarai,\* Luca Bergamini, Eneko Lopez, Maria Carmen Morant-Miñana, Jost Adam, Nerea Zabala, Javier Aizpurua, and Andreas Seifert\*

Multivariate analysis applied in biosensing greatly improves analytical performance by extracting relevant information or bypassing confounding factors such as nonlinear responses or experimental errors and noise. Plasmonic sensors based on various light coupling mechanisms have shown impressive performance in biosensing by detecting dielectric changes with high sensitivity. In this study, gold nanodiscs are used as metasurface in a Kretschmann setup, and a variety of features from the reflectance curve are used by machine learning to improve sensing performance. The nanostructures of the metasurface generate new plasmonic features, apart from the typical resonance that occurs in the classical Kretschmann mode of a gold thin film, related to the evanescent field beyond total internal reflection. When the engineered metasurface is integrated into a microfluidic chamber, the device provides additional spectral features generated by Fresnel reflections at all dielectric interfaces. The increased number of features results in greatly improved detection. Here, multivariate analysis enhances analytical sensitivity and sensor resolution by 200% and more than 20%, respectively, and reduces prediction errors by almost 40% compared to a standard plasmonic sensor. The combination of plasmonic metasurfaces and Fresnel reflections thus offers the possibility of improving sensing capabilities even in commonly available setups.

## 1. Introduction

Surface plasmon resonance (SPR) biosensors are widely used for optical sensing in biology, microbiology, biochemistry, and medical sciences. They provide rapid, non-invasive, and high-sensitivity detection, with possible real-time analysis, and they are used to monitor binding conditions between molecules, viruses, or bacteria.<sup>[1–4]</sup> Nowadays, the primary optical excitation method in commercial SPR systems includes the attenuated total internal reflection that generates an evanescent wave, such as in a typical Kretschmann configuration, where a high-index prism serves as a coupling medium to match energy and momentum of incoming photons with metal electrons to generate surface plasmon polaritons (SPPs). The limit of detection of SPR systems is about several  $\text{pg}\cdot\text{mm}^{-2}$ , which is two orders of magnitude better than standard detection methods.<sup>[5]</sup> Although SPR is a powerful and highly sensitive biosensing technique, it has not yet

J. Etxebarria-Elezgarai, E. Lopez, A. Seifert  
CIC nanoGUNE BRTA  
Tolosa Hiribidea 76, San Sebastian 20018, Spain  
E-mail: [j.etxebarria@nanogune.eu](mailto:j.etxebarria@nanogune.eu); [a.seifert@nanogune.eu](mailto:a.seifert@nanogune.eu)  
L. Bergamini, N. Zabala, J. Aizpurua  
Department of Electricity and Electronics  
FCT-ZTF  
UPV/EHU  
Bilbao 48080, Spain  
L. Bergamini, N. Zabala, J. Aizpurua  
Materials Physics Center  
CSIC-UPV/EHU and DIPIC  
San Sebastian 20018, Spain

E. Lopez  
Department of Physics  
University of the Basque Country (UPV/EHU)  
San Sebastian 20018, Spain  
M. C. Morant-Miñana  
Centre for Cooperative Research on Alternative Energies (CIC energiGUNE)  
Basque Research and Technology Alliance (BRTA)  
Alava Technology Park  
Albert Einstein 48, Vitoria-Gasteiz 01510, Spain  
J. Adam  
Computational Materials and Photonics (CMP)  
Department of Electrical Engineering and Computer Science  
University of Kassel  
34121 Kassel, Germany  
J. Aizpurua, A. Seifert  
IKERBASQUE  
Basque Foundation for Science  
Euskadi Plaza 5, Bilbao 48009, Spain

 The ORCID identification number(s) for the author(s) of this article can be found under <https://doi.org/10.1002/smt.d.202301445>

DOI: 10.1002/smt.d.202301445

reached its full potential. The sensitivity cannot be improved beyond a specific limit due to limitations imposed by light-matter interactions, which gives rise to purely propagating SPPs on a flat metal surface.<sup>[5,6]</sup> The metal surface usually consists of noble metals such as gold (Au) or platinum, semi-noble metals such as copper or silver, or aluminum.

One alternative for enhanced sensitivity, reported in the literature, relies on the modification of the physical properties of the surface plasmons by employing metamaterials composed of plasmonic nanostructures hosting localized surface plasmon resonances (LSPRs). Some examples of plasmonic metamaterials include plasmonic nanorods,<sup>[7]</sup> nanoslits<sup>[8]</sup> and nanodot arrays,<sup>[9]</sup> 3D plasmonic crystals<sup>[10]</sup> or graphene-Au metasurfaces.<sup>[11]</sup> These designed materials open the way for developing devices with detection sensitivities down to single molecules and provide new biosensor technology. Nonetheless, these new plasmonic devices require complex fabrication processes, with increased manufacturing time and costs, resulting in difficult commercialization since they are very specific with respect to their application. From a fabrication point of view, Au is the preferred material for plasmonic metamaterials in biosensors, first, because the functionalization process of Au surfaces for biosensing applications is well established,<sup>[12]</sup> second, because the nanofabrication techniques with this material have experienced significant advances during the last years,<sup>[13]</sup> and third, because of its chemical stability. Direct writing techniques like electron beam or ion beam lithography can be used to obtain nanostructures with nanometer-sized gaps.

Among the strategies to improve the sensitivity of SPR sensors, nanostructured gratings of noble metals have demonstrated successful results.<sup>[14–17]</sup> In 2D periodic arrangements of nanostructures, surface lattice resonances (SLRs) can be excited due to in-plane diffracted light, in addition to LSPRs excited in the nanostructures, which act as nanoantennas.<sup>[16]</sup> When coupled to resonant plasmonic nanostructures, these SLRs provide sharp optical features in the optical response of the system that can be exploited for achieving enhanced sensitivity and resolution.<sup>[18–20]</sup>

In addition, when the dielectric-plasmonic interface is operated in Kretschmann configuration, the evanescent field created beyond the angle of total internal reflection (TIR) can couple to the nanostructures in analogy to propagating plasmons in continuous metal layers, leading to SPP-like resonances.

All these plasmonic effects and their coupling depend on the material, size, shape, arrangement, and environment of single plasmonic nanostructures.<sup>[21–23]</sup>

While conventional data analysis considers a single feature of the plasmonic response in the reflectance curve, such as the angular resonance shift, multivariate data analysis (MVA) methods do collect more information from the reflectance curves. Hence, as demonstrated in a recent work,<sup>[24]</sup> MVA allows considerable improvement in data analysis compared to univariate analysis (UVA) by optimizing (non)linear combinations of many characteristic features or variables of the SPR curves.

Our work introduces a MVA approach for improving the current SPR technology toward better sensitivity and resolution. The proposed SPR device comprises metamaterials as Au nanoparticle arrays, patterned on top of a glass substrate and integrated into a microfluidic chamber made of polymeric layers. We optically excite the SPR device in Kretschmann configura-

tion by monochromatic laser light. The array of Au nanodiscs induces diffraction effects owing to the lattice,<sup>[25]</sup> LSPRs rooted in the finite size of the plasmonic nanostructures and a material-dominated SPP-like resonance due to the evanescent field at an angle where energy and momentum match the resonance condition. At the same time, the light transmitted through the Au nanodisc layer interacts with the different dielectric interfaces of the whole sensing device, including the layers constituting the microfluidic chamber, the analyte, and surrounding air, leading to multiple Fresnel reflections. The measured reflected light shows a complex structure in its angle-dependent curve, associated with plasmonic resonances at the metallic nanograting and multiple Fresnel reflections generated at the different dielectric interfaces. As a result, the reflectance curve presents multiple dips, whose numerous features are exploited by MVA and compared to a standard plasmonic sensor based on a continuous Au layer.

## 2. Experimental Section and Methods

### 2.1. SPR System Configuration

The SPR optical system was set up in Kretschmann configuration, where p-polarized laser light of  $\lambda = 632.8$  nm enters the system through a high refractive index cylindrical prism (SF57,  $n = 1.8396$ ) and a BK7 substrate ( $n = 1.5151$ , thickness 0.17 mm), before exciting the plasmonically active Au nanostructure. The incident laser light always stroked the curved cylindrical surface of the prism at normal incidence, that is, without refraction. A custom MATLAB software controls rotational stages and detectors, as described in a previous work.<sup>[24]</sup> **Figure 1** shows a schematic of the proposed plasmonic device in Kretschmann configuration. An analyte covered the metasurface and is separated from the environment (air) by a PMMA layer of thickness 175  $\mu\text{m}$ .

### 2.2. Fabrication of the Nanostructured SPR Device

The plasmonic device was fabricated as a nanostructured grating on a 170  $\mu\text{m}$  BK7 glass substrate. First, a grating pattern in ZEP20A resist was written by electron beam lithography (EBL) in a RAITH150Two EBL system (Dortmund, Germany) at 20 kV beam energy, 30  $\mu\text{m}$  aperture, 10.5 nm working distance, and  $20 \times 20 \mu\text{m}^2$  writing field. Then, a 50 nm-thin Au layer was deposited on the structure by physical vapor deposition, using a two nm-thick titanium interlayer as an adhesion layer. Finally, a lift-off process delivered the desired nanostructures (nanodiscs), as shown in **Figure 1c**, realized by immersing the substrate in ZED developer and rinsing it with acetone. The nanostructured grating consisted of a nanodisc array, with disc diameters  $D = 200$  nm and height  $h = 50$  nm, arranged with a 2D grating period  $P = 300$  nm (hereafter design *P300D200h50*).

For comparison, a standard plasmonic device, consisting of a 50 nm continuous Au layer, was fabricated by direct physical vapor deposition on top of a 170  $\mu\text{m}$  BK7 glass substrate, using a titanium binding layer of 2 nm. Subsequently, the nanostructured substrate was integrated into a microfluidic chamber manufactured by polymer layer lamination, as described in<sup>[24]</sup> and shown in **Figure 1d**.

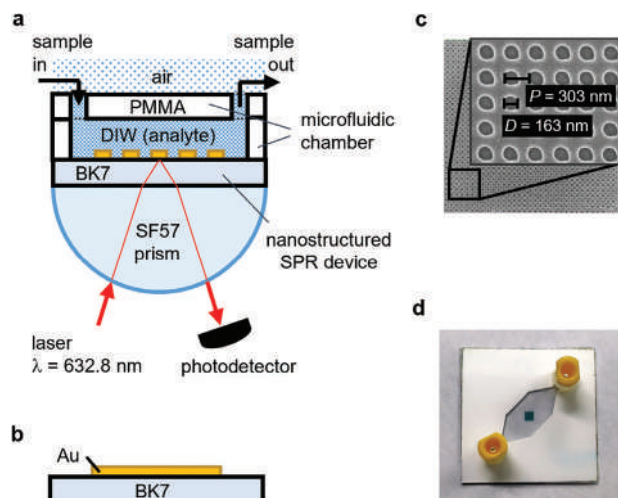


**Figure 1.** Optical, plasmonic, and fluidic elements of the developed SPR sensor: a) Schematic of the plasmonic setup in Kretschmann configuration (image not to scale) consisting of an excitation laser ( $\lambda = 632.8$  nm), a coupling prism, and the SPR device comprised of a nanostructured Au metasurface for enhanced surface plasmon resonance sensing. b) Standard plasmonic sensor based on a continuous gold layer, which only renders SPPs.<sup>[24]</sup> c) SEM image of a plasmonically active 2D Au nanodisc grating fabricated by electron beam lithography on top of a BK7 glass substrate; Inset: zoom in of the nanograting. d) Final  $22 \times 22$  mm<sup>2</sup> SPR device, including the nanodisc metamaterial of  $1.5 \times 1.5$  mm<sup>2</sup> on a glass substrate and the microfluidic chamber composed of dielectric layers.

### 2.3. Electromagnetic Simulations

Finite-element method (FEM) simulations were carried out to design the final nanostructured grating with an optimal plasmonic response shown in this manuscript. This work utilized the commercially available software package COMSOL Multiphysics. A schematic representation of the light path through the plasmonic substrate is presented in **Figure 2**. Given the large coupling prism size (radius of 40 mm) and the thick BK7 glass substrate (thickness of 170  $\mu$ m), as compared to the nanostructures (height  $h$  of tens of nm), as well as the entire integrated device comprising microfluidics and polymeric housing, the original dimensions comprised a severe multi-scale nature. This multi-scale characteristic cannot be covered fully by discretization-based simulations due to the vast computational capacity. Therefore, initial simulations for 1D and 2D structures (thin films and 1D-Gratings) were conducted with a semi-analytic, in-house-developed rigorous coupled-wave analysis (RCWA) code. These simulations revealed that including all-dielectric interfaces at realistic distances only introduces a multitude of back- and forward reflections and Fabry-Perot resonances. In the final model, fully analytic Fresnel corrections were consequently considered for the large layer influence and only considered a short interface range between the BK7/Au/analyte in the FEM calculations (Figure 2b). The FEM-simulated result was subsequently corrected via Snell's law to include the interface effects between the BK7 glass substrate and the SF57 coupling prism and between the prism and the surrounding air, as shown in Figure 2c.

The optical material properties used in this study were defined by their complex refractive indices at  $\lambda = 632.8$  nm. For the BK7

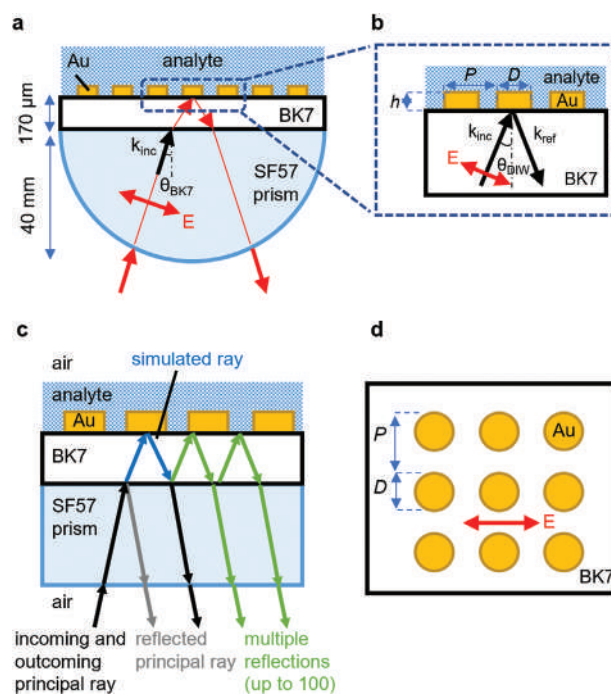


**Figure 2.** Schematics of the SPR system considered in the electromagnetic simulations (sketches not to scale). a) Representation of the plasmonic substrate with 2D grating, which is attached to the coupling prism of the Kretschmann configuration; the microfluidic chamber is not considered. b) Simulation box, which considers the light interactions only in a short range near the Au nanostructures; period  $P = 300$  nm, disc diameter  $D = 200$  nm, height  $h = 50$  nm. c) Light propagation within the system considering multiple reflections at both air/SF57 and SF57/BK7 interface. d) Top view of the simulated periodic Au nanostructure composed of circular nanodiscs.

glass substrate, SF57 coupling prism, air media, and analyte media, refractive index values of 1.5151, 1.8396, 1.0, and 1.332 (for water) were used, respectively; for the Au and Ti binding layer, the complex refractive indexes  $n_{\text{Au}} = 0.1941 + 3.5932i$ <sup>[26,27]</sup> and  $n_{\text{Ti}} = 2.70421 + 3.765614i$ <sup>[27,28]</sup> were employed, respectively. The optical response was calculated for a broad range of incident angles, using an incident plane wave with  $\lambda = 632.8$  nm in Kretschmann configuration and for varying analyte refractive index  $n$ . Several nanogratings were simulated with different nanostructure heights, sizes, shapes, and pitches to find the optimum nanostructure design. Due to the enhanced simulation speed of time-domain methods, this work roughly investigated these influences with finite-difference time-domain (FDTD) simulations (see Supporting Information) before simulating the finally chosen structure with the enhanced accuracy of the FEM-intrinsic non-cartesian grids.

As mentioned above, the electromagnetic calculations cannot consider the whole sensing device but only the plasmonic metasurface, attached to the coupling prism and in contact with the analyte sample under test. Additionally, the light back-reflected to the detector after traveling through the integrated system,  $R_{\text{T}}$ , is estimated as the sum of back reflections from all-dielectric interfaces,  $R_{\text{i}}$ , using Fresnel's equations for p-polarized light,

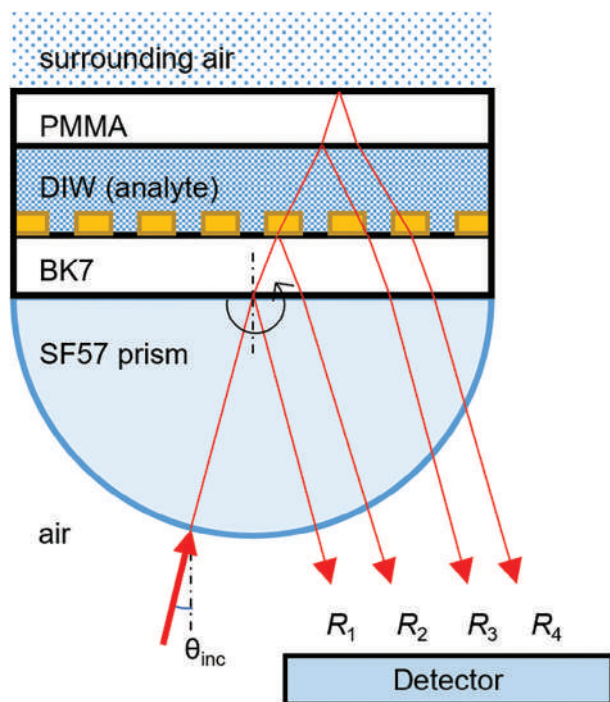


**Figure 3.** Schematic of the transmitted and reflected light at each dielectric interface involved in the SPR system operated in Kretschmann configuration (image not to scale); multiple reflections are not displayed in this picture.

where also all multiple reflections must be considered, that is,

$$R_T = \sum R_i \quad (1)$$

$$R_i = \left| \frac{n_i \sqrt{1 - \left(\frac{n_i}{n_{i+1}} \sin \theta_i\right)^2} - n_{i+1} \cos \theta_i}{n_i \sqrt{1 - \left(\frac{n_i}{n_{i+1}} \sin \theta_i\right)^2} + n_{i+1} \cos \theta_i} \right|^2 \quad (2)$$

where  $n_i$  and  $n_{i+1}$  represent the refractive indices before and behind the  $i$ th interface, respectively; and  $\theta_i$  is the angle of incidence at the interface. The back reflections at the outer dielectric interfaces encountered between the different dielectric layers that form the microfluidic chamber (i.e.,  $R_3$  and  $R_4$  in **Figure 3**) were not considered in the calculations, as they do not severely affect the signal obtained. The final simulation model (**Figure 4b**) comprised a weighted superposition of stack-based fully analytic Fresnel response from (1) and (2), and high-accuracy FEM simulations for the local plasmonic effects. This model reproduced and explained the fundamental experimental results' nature well. This work addressed the remaining discrepancies to the missing multiple reflections introduced by the real stack and by imperfections of the fabricated metasurface.

## 2.4. Plasmonic Measurements

Two plasmonic device configurations were analyzed in Kretschmann configuration: one device as reference comprised

a 50 nm thick continuous Au layer, and the other consisted of a 50 nm thick nanostructured Au grating (see **Figure 1a,b**). The plasmonic devices were attached to the prism using an index-matching oil ( $n = 1.516$ ). A 3D-printed holder aligned the nanostructured grating with the incident laser. Reflectance curves were measured for the two plasmonic device configurations using five different aqueous solutions of increasing sucrose concentrations, from 0% to 10%, to provide different refractive index (RI) values. The RI values of sucrose solutions were measured using a commercial refractometer (digital refractometer PCE-DRH1 series, PCE instruments, Alicante, Spain). RI values of 1.333, 1.3359, 1.3403, 1.3446, and 1.3475 were obtained for sucrose solutions of 0%, 2%, 5%, 8%, and 10%, respectively. The SPR curves were measured by angle interrogation between  $43^\circ$  and  $56^\circ$  with a sampling of  $0.004^\circ$ . For each sucrose concentration and device architecture, 20 measurements were carried out.

## 2.5. Multivariate Data Analysis

Multivariate analysis was used to compare the performance of the proposed sensor based on nanostructured Au with a standard SPR device based on a continuous Au layer. Partial least squares (PLS) was used to build the multivariate calibration models for the two different SPR device configurations, using multiple curve features around the dips encountered in the reflectance curves. Three MVA models were built for the nanostructured Au grating: one individual model was generated for each of the two dips of interest as a performance indicator, and the third model combined the parameters of both dips. These three models were compared with a fourth MVA model built for a continuous Au layer containing a single resonance dip. The evaluation of the PLS multivariate calibration models, and the comparison between them to find the best model, is done using four analytical figures of merit (AFOMs): *sensitivity* (SEN), *analytical sensitivity* ( $\gamma$ ), *root mean square error of prediction* (RMSEP) and *resolution* ( $r_{\text{Sensor}}$ ), as defined in the former study.<sup>[24]</sup> SEN measured the variation of the multivariate sensor signal for changes in the refractive index, which is the slope of the multivariate calibration curve based on the regression coefficients.  $\gamma$  determines the ratio between SEN and RMSEP, where RMSEP estimates the prediction uncertainty. Finally,  $r_{\text{Sensor}}$  represents the minimum detectable refractive index change. Multivariate algorithms were used in MATLAB to build the multivariate calibration models using Monte Carlo methods for cross-validation and Haaland and Thomas criterion for the prediction of the optimum number of latent variables.<sup>[29]</sup> The data normalization to unity was done using the mean normalization for each feature.

## 3. Results and Discussion

**Figure 4a,b** compare simulated and experimentally measured reflectance curves for continuous and nanostructured Au layers of design P300D200h50, respectively, using deionized water as the analyte. The optimum nanostructure design of P300D200h50 was calculated by FEM and FDTD simulations (see Supporting Information for further details about nanostructure design

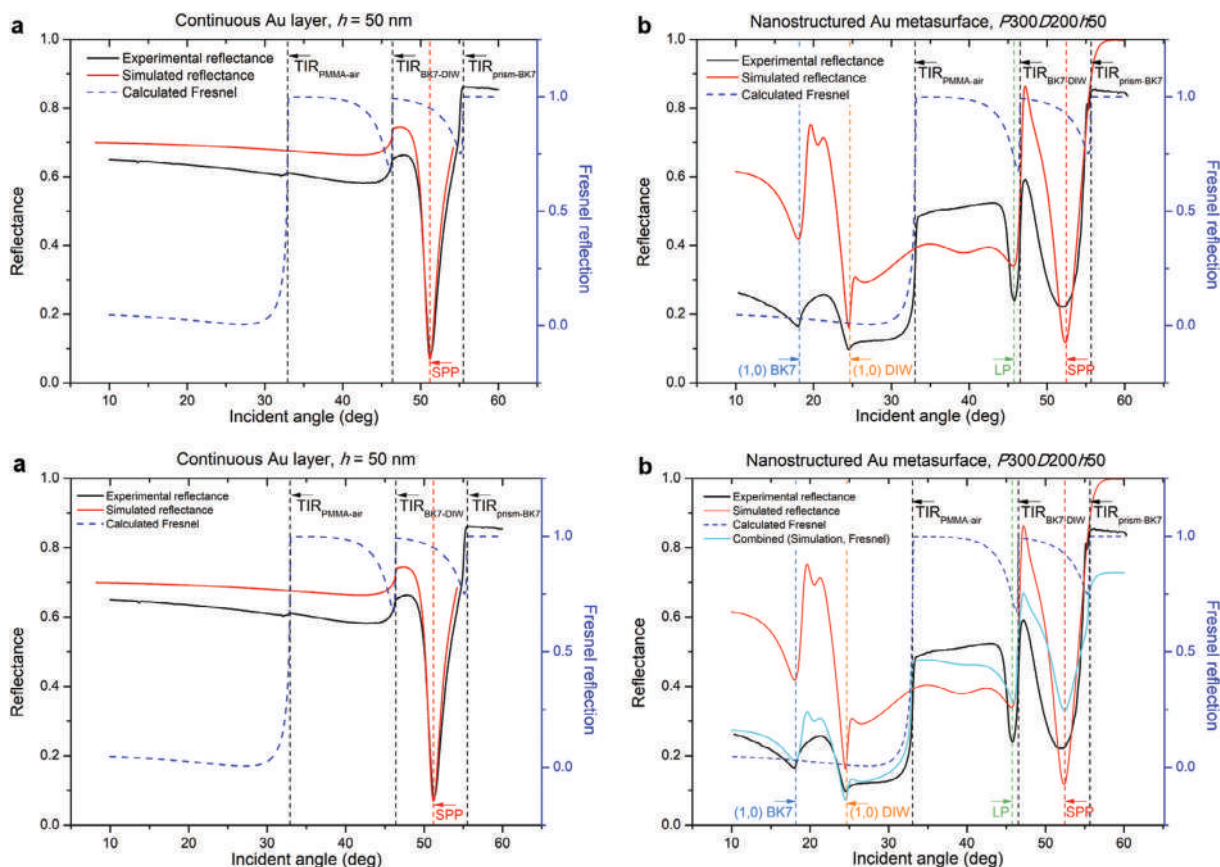


**Figure 4.** Comparison between the simulated plasmonic response (red), the theoretical calculation of back reflections by Fresnel equations without multiple reflections (dashed blue), and the experimentally measured reflectance as a function of the incident angle (black), using deionized water as analyte. a) Continuous Au layer of height  $h = 50$  nm. b) Nanostructured Au grating of design P300D200h50. The cyan curve illustrates a weighted combination of stack-based analytic Fresnel response and high-accuracy FEM simulations for the local plasmonic effects. The theoretical angular positions of the diffraction modes calculated by simulations are indicated with colored vertical dashed lines. Additionally, the angular positions where total internal reflection occurs between the different dielectric interfaces, as detailed in Figure 3, are indicated as  $TIR_{\text{interface1} / \text{interface2}}$ .

optimization). Four plasmonic resonances (dips) are identified, located at  $\approx 18^\circ$ ,  $24.5^\circ$ ,  $45.6^\circ$ , and  $52.3^\circ$ , and indicated in Figure 4b as dashed vertical lines in blue, orange, green, and red.

The experimental reflectance widely agrees with the results obtained in the simulations. It shows a much more complex curve progression for the nanostructures than for the continuous Au layer, which features a single resonance dip. However, when nanostructures are present, a complete explanation of the experimental curve requires consideration of all Fresnel reflections at the various dielectric interfaces of the entire integrated macroscopic sensing device, as detailed in Figure 3. These reflections have not been included in the FEM calculations due to the multiscale dimensions of the microfluidic chamber and the PMMA cover, which are several orders of magnitude larger than the size of the nanostructures. The major differences between the experimental and the simulated result are (i) the increase in the reflected light intensity at  $32.93^\circ$  due to TIR at the interface between the PMMA cover layer and the atmospheric air (this increase is very little for the continuous layer due to the mirror-like effect of the Au layer, which reflects almost all the incident light, even at small incident angles); and (ii) an additional dip occurring at  $46.1^\circ$ , which is a result of the complex combination of

all Fresnel reflections, as described in Section 2.3, and indicated in Figure 4 by the analytically calculated dashed blue curves. This dip, caused by Fresnel reflections, together with the plasmon resonance at  $45.6^\circ$ , generates a double dip in the resonance curve, which can be observed in the figures with higher resolution (later in Figures 6b and 7b).

In Figure 5 we showcase the near-field maps found at the angles corresponding to the dips in the spectrum. The dips  $\approx 18^\circ$  and  $24.5^\circ$  are related to the (1,0) diffraction order of the nanograting. The dip at  $18^\circ$  reveals a plasmon resonance mostly located at the Au-glass interface, since the plasmon of each particle interacts with the other particle plasmon through the BK7 substrate (we call it (1,0) BK7 mode).<sup>[8]</sup> In contrast, the dip at  $24.5^\circ$  shows a plasmonic field mainly concentrated at the metal-analyte and the diffraction coupling takes place through the surrounding medium (we call it (1,0) DIW mode). Owing to the different nature of these modes, the latter is more likely to be sensitive to refractive index changes of the analyte than the former. These features are the result of the coupling of single nanostructure plasmonic resonances with in-plane diffracted light due to the periodic lattice configuration. We note that, due to the circular nanostructure shape, the plasmonic resonances appear as

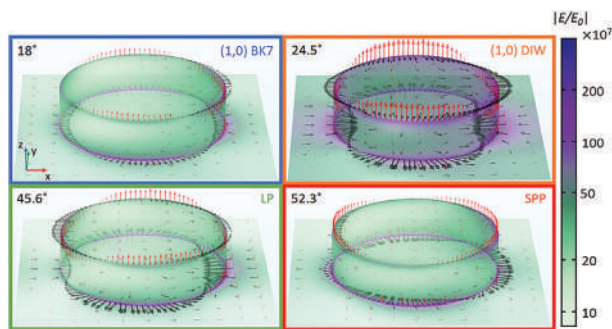


**Figure 5.** Simulated near-field maps corresponding to the resonance positions marked by the colored vertical dashed lines in Figure 4b. The local electric field magnitude  $|E|$  [V/m] on the particle surface and the substrate surface (BK7-analyte interface), are normalized with the exciting electric field intensity  $|E_0|$ . The red and black arrows visualize the normalized local electric field strength (logarithmically scaled for better visibility) perpendicular to and in-plane with the substrate, ( $E_z$ -direction) and ( $E_{xy}$ -plane), respectively. Since the excitation is strictly transverse-magnetic (the  $E$ -field lies in the  $x$ - $z$ -plane), the plots reveal a strong polarization-turning behavior due to the circular particle shape, most prominently visible in the strong-shifting modes at  $24.5^\circ$  ((1,0) DIW) and  $45.6^\circ$  (LP) angle of incidence. Both resonances reveal a strong, ring-shaped resonance at the top particle surface.

ring-shaped localized surface plasmon resonance: While the incident light is strictly transverse-magnetic (the  $E$ -field lies in the  $x$ - $z$ -plane), the plots in Figure 5 (black arrows) reveal a strong polarization-turning behavior, most prominently visible in the strong-shifting modes at  $24.5^\circ$  ((1,0) DIW) and  $45.6^\circ$  (LP localized plasmons) angle of incidence. The dip  $\approx 52.3^\circ$  (marked with a vertical dashed red line in Figure 4a,b) is the equivalent of the excitation of a propagating surface plasmon polariton (SPP) in continuous layers and results from the evanescent field that propagates at the metal-analyte interface at angles larger than the angle of total internal reflection (again, degeneration happens due to the nanostructure morphology). Consequently, this plasmonic resonance is also potentially sensitive to refractive index changes. The investigation of the electric (vector) fields on the nanoparticle and the substrate surfaces additionally reveals that the refractive index-sensitive resonances at  $24.5^\circ$  ((1,0) DIW) and  $45.6^\circ$  (LP) exhibit strong ring-shaped resonant states on the upper nanodisc surface, whereas the less sensitive resonances at  $18^\circ$  and  $52.3^\circ$  exhibit non-resonant and dipole-like (between the upper and lower particle edge) near-field states, respectively. We ascribe the stronger sensitivity to analyte refractive index changes to these resonances.

Figure 6a shows the simulated reflectance curves for the P300D200h50 nanostructured Au metasurface for varying analyte refractive indices. Figure 6b compares experimental reflectance curves in the range of  $42^\circ$ – $56^\circ$  for a 50 nm thick continuous Au layer and for a P300D200h50 nanostructured Au metasurface, using increasing values of refractive index for the analyte. In the experimental study, we focus on a higher angular region ( $42^\circ$ – $56^\circ$ ) because, according to the near-field maps, the dip  $\approx 18^\circ$  is not very sensitive to refractive index changes of the analyte, and thus is not taken into account in the model, and the dip  $\approx 24^\circ$  has a narrow and shallow shape with a low signal-to-noise ratio (see Figure 4b), so it is not possible to use

multiple features for the multivariate model. Therefore, for the multivariate calibration model, we focus on the two dips around the TIR between the glass substrate and the analyte, which allows us to perform fast scans within a small angular range. As mentioned above, the dips  $\approx 46^\circ$  and  $52^\circ$  include both plasmonic and Fresnel reflection features that are highly sensitive to changes in the refractive index of the analyte. The reflectance dip  $\approx 46^\circ$  shows that the two overlapping phenomena—plasmonic dip predicted at  $45.6^\circ$  by the electromagnetic simulations and Fresnel reflections at  $46.1^\circ$ —create a double-dip feature, which is highly sensitive to analyte refractive index changes, as seen in Figure 6b. The localized SPP dip of the nanostructured Au metasurface  $\approx 52^\circ$  is the counterpart of the resonance condition for the continuous Au layer and appears at the same angular position. By reducing the length of a continuous layer and substituting it with multiple discrete nanostructures (Au nanodiscs in this case), the resulting resonance dip becomes broader and less deep, as shown in Figure 6b. The changes in the experimental reflectance curve due to variations in the analyte refractive index allow us to exploit multiple parameters from these three dips for the analysis of the performance of the entire sensing element.

The characteristic features of the dips shown in Figure 6b are extracted according to Figure 7 to build the calibration models that allow performance evaluation of the two sensing devices under analysis. For the continuous Au layer, the characteristic features considered for building the multivariate calibration model include the maximum extinction  $A$ , the slope  $S$  at half  $A$  before the resonance condition, the angular position of this slope  $\theta_S$ , the resonance angle  $\theta_{\text{SPR}}$ , the curvature  $\kappa_{\text{SPR}}$  at resonance, and the angular distance between  $\theta_S$  and  $\theta_{\text{SPR}}$  resonance ( $\Delta\theta_{\text{SPR-S}}$ ), which we denote as *half width at half maximum* HWHM for simplicity (Figure 7a).

For the nanostructured Au grating, the characteristic reflectance curve shows two dips around the TIR angle (Figure 6b). For the dip on the right, which is the equivalent of the resonance of the continuous Au layer, the calculated features are the same:  $A$ ,  $S$ ,  $\theta_S$ ,  $\theta_{\text{SPR}}$ ,  $\kappa_{\text{SPR}}$ , and HWHM. The dip on the left consists of two local dips (see Figure 7b) that are described with three extinction amplitudes  $A_1$ ,  $A_2$ , and  $A_3$ , three angular positions  $\theta_{R1}$ ,  $\theta_{R2}$ , and  $\theta_{R3}$  around the minimum, the slope  $S$  at half maximum extinction  $A_1 + A_2$  before the minimum at  $\theta_{R1}$ , the angular position of this slope  $\theta_S$ , the HWHM, the steepest negative slope  $S_{\text{min,R2-R3}}$  before the minimum at  $\theta_{R3}$  (between angular positions  $\theta_{R2}$  and  $\theta_{R3}$ ), the angular position of this steepest slope  $\theta_{\text{Smin}}$ , the angular distance between the steepest slope and the minimum reflectance condition  $\Delta\theta_{R3-S_{\text{min}}}$  or also called half width at slope minimum HWSM, and finally three curvatures  $\kappa_{R1}$ ,  $\kappa_{R2}$ , and  $\kappa_{R3}$  at angular positions  $\theta_{R1}$ ,  $\theta_{R2}$ , and  $\theta_{R3}$ .

The univariate calibration curves depicted in Figures S5–S7, Supporting Information show the variation of each mean-normalized feature as a function of the RI of the analyte. In general, a higher standard deviation (uncertainty) can be observed for derivatives as significant features, such as the slopes  $S$  and  $S_{\text{min}}$  or the curvatures  $\kappa_{\text{SPR}}$ ,  $\kappa_{R1}$ ,  $\kappa_{R2}$ , and  $\kappa_{R3}$ , whereas the features of extinction depth  $A$ ,  $A_1$ ,  $A_2$ , and  $A_3$  and angular positions  $\theta_{\text{SPR}}$ ,  $\theta_{R1}$ ,  $\theta_{R2}$ ,  $\theta_{R3}$ ,  $\theta_S$ ,  $\theta_{\text{Smin}}$  show smaller uncertainties.

The results of the MVA analysis for each PLS model are summarized in Table 1, Figures 8 and 9. In total, four multivariate models are built: three for the P300D200h50 nanostructured Au

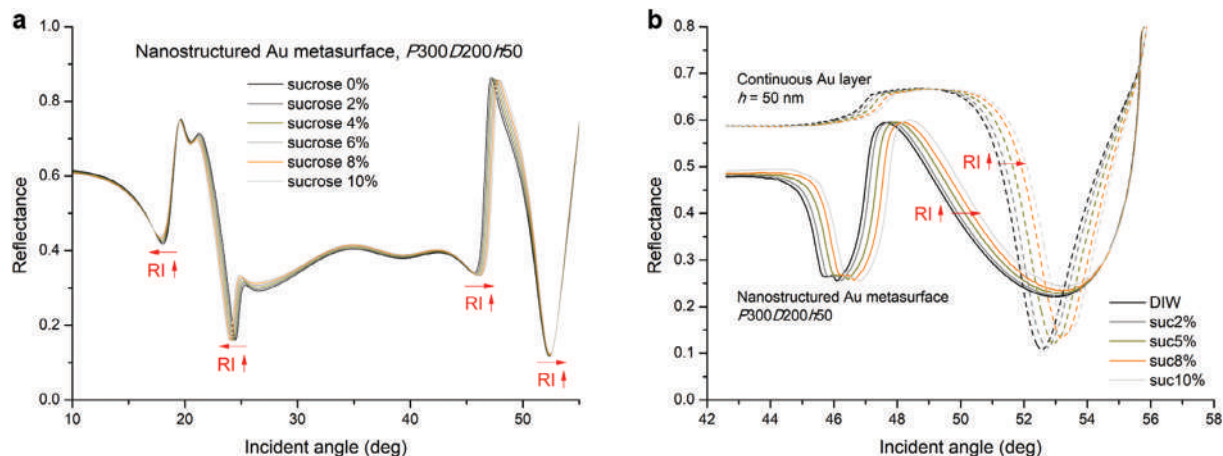


**Figure 6.** Theoretical and experimental study of an SPR device. a) Simulated plasmonic response as a function of the incident angle for a P300D200h50 nanostructured Au metasurface for different sucrose concentrations of the analyte. b) Experimental reflectance for a 50 nm thick continuous Au layer (dotted lines) and a P300D200h50 nanostructured Au metasurface (solid lines) for increasing concentrations of sucrose (0%, 2%, 5%, 8%, 10%), and hence, increasing values of  $n$ .

metasurface (PLS1, PLS2, and PLS3) and one for the 50 nm thick continuous Au layer (PLS4). Calibration model PLS1 uses the parameters from the double-dip  $\approx 46^\circ$  related to Fresnel reflections and plasmonic resonance, while PLS2 uses the parameters from the localized SPP resonance  $\approx 52^\circ$ . Model PLS3 combines the parameters of these two dips, yielding a sensor that combines Fresnel reflections with plasmonics.

The statistical errors observed for each individual parameter in the univariate calibration curves are reflected in the regression coefficients obtained from the PLS multivariate calibration models shown in Figure 8. The regression coefficients evaluate the relevance of the individual variables by generating a linear combination of original features, such that the covariance is maximized, and the root mean square error of cross-validation (RMSECV) and the root mean square error of prediction (RMSEP) are optimized. Therefore, the features with lower standard de-

viation have a greater contribution in the multivariate models, which is represented by larger absolute values of the regression coefficients.

The resonance dips for the continuous layer and the nanostructured metasurface  $\approx 52^\circ$  lead to a similar relevance of the characteristic features, as shown in Figure 8b,d. However, smaller standard deviations are calculated by UVA for features of the continuous layer, which are related to sharper SPR resonances. As a result, this can be seen in the MVA calibration errors in Table 1, where smaller RMSECV is achieved for the continuous Au layer (PLS4) than for the nanostructured Au grating (PLS2).

Table 1 and Figure 9 gather the AFOMs calculated for PLS multivariate calibration models for both devices, three for the P300D200h50 nanostructured Au metasurface and one for the continuous Au layer, as well as the statistical and prediction analysis for these four models. The analytical sensitivity  $\gamma$  combines

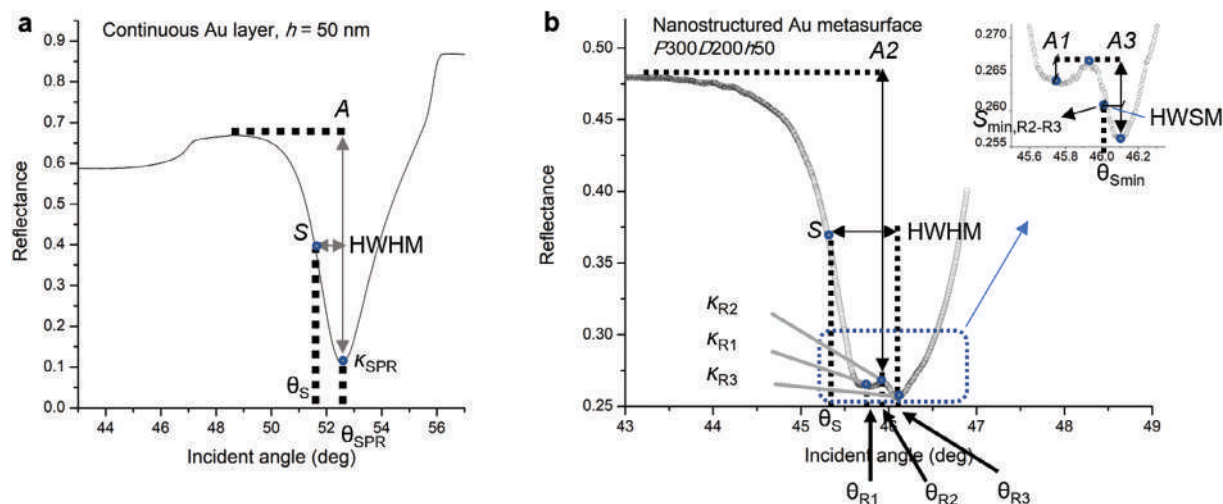


**Figure 7.** Definition of SPR features for multivariate data analysis. a) Characteristic parameters of the plasmonic response of a continuous Au layer to build a multivariate calibration model:  $A$ ,  $S$ ,  $\theta_S$ ,  $\theta_{SPR}$ ,  $\kappa_{SPR}$ , and HWHM. b) Close-up view of the double-dip  $\approx 46^\circ$  for the P300D200h50 nanostructured Au metasurface with characteristic parameters  $A_1$ ,  $A_2$ ,  $A_3$ ,  $\theta_{R1}$ ,  $\theta_{R2}$ ,  $\theta_{R3}$ ,  $S$ ,  $\theta_S$ , HWHM,  $S_{min,R2-R3}$ ,  $\theta_{Smin}$ , HWSM,  $\kappa_{R1}$ ,  $\kappa_{R2}$  and  $\kappa_{R3}$ .

**Table 1.** Summary of the statistical cross-validated results and the calculated AFOMs from a multivariate PLS inverse calibration model. The multivariate analysis includes results for the multiple Fresnel reflection-plasmonic dips obtained from the nanostructured plasmonic device of design P300D200h50 and the single resonance dip obtained from the plasmonic device based on a 50 nm thick continuous Au layer.

MVA calibration results	Nanostructured Au metasurface P300D200h50			Continuous Au layer
	PLS1	PLS2	PLS3	PLS4
RMSECV [RIU]	$1.12 \times 10^{-04}$	$3.48 \times 10^{-04}$	$1.26 \times 10^{-04}$	$1.42 \times 10^{-04}$
Optimum n° of latent vectors	12	4	11	5
	AFOMs			
$\gamma$ [RIU <sup>-2</sup> ]	$8.02 \times 10 + 05$	$3.20 \times 10 + 05$	$1.47 \times 10 + 06$	$4.93 \times 10 + 05$
RMSEP [RIU]	$9.38 \times 10^{-05}$	$2.98 \times 10^{-04}$	$9.22 \times 10^{-05}$	$1.48 \times 10^{-04}$
$r_{\text{Sensor}}$ [RIU]	$1.27 \times 10^{-06}$	$2.32 \times 10^{-06}$	$1.83 \times 10^{-06}$	$1.65 \times 10^{-06}$

RIU: refractive index units.

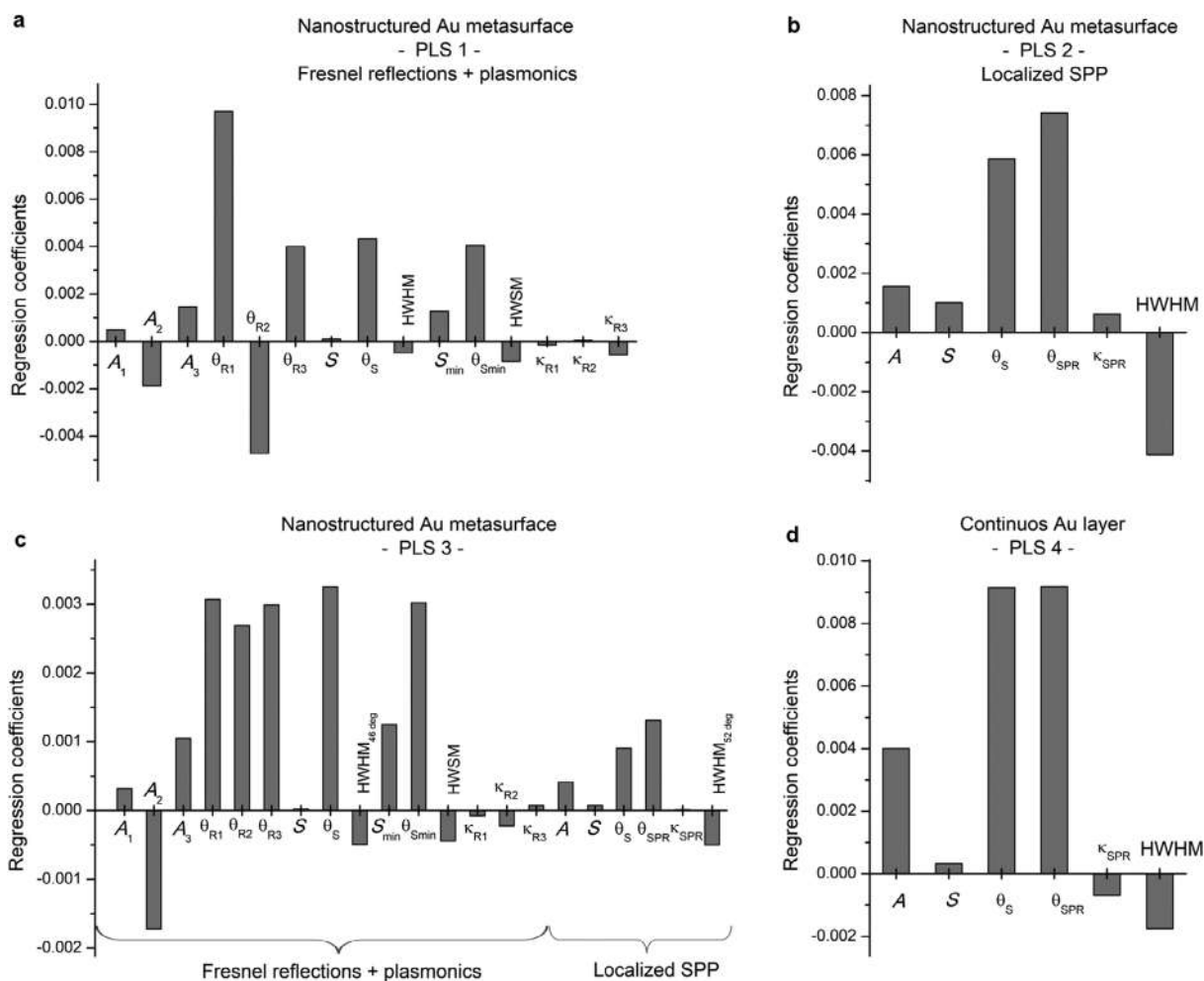


**Figure 8.** Normalized regression coefficients estimated by the PLS multivariate model for the two plasmonic devices and their corresponding dips. a–c) Nanostructured Au metasurface of design P300D200h50. a) PLS1 for the double dip  $\approx 46^\circ$  that considers Fresnel reflection and plasmonic features, b) PLS2 for the localized SPP resonance  $\approx 52^\circ$ , c) PLS3 for the combination of both dips  $\approx 46^\circ$  and  $52^\circ$ ; d) PLS4 for the resonance dip of the continuous Au layer.

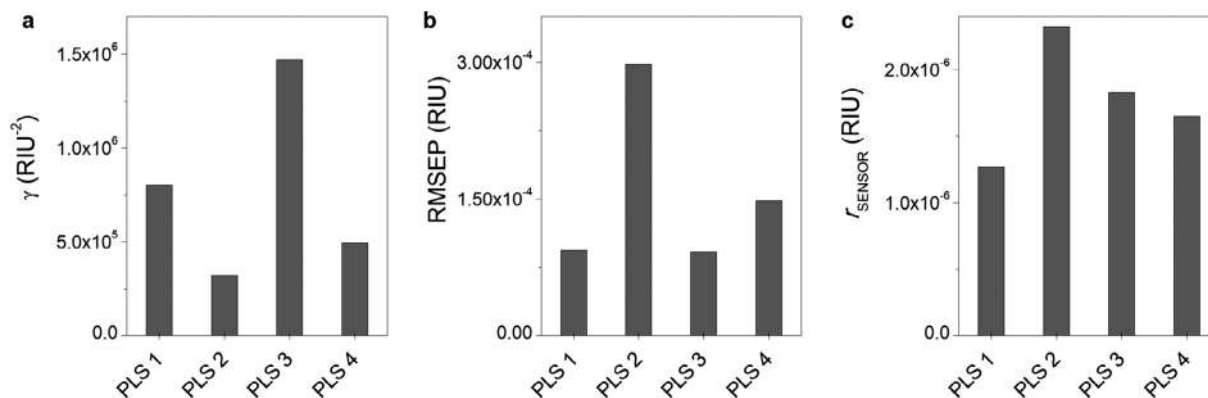


**Figure 9.** Figures of merit obtained from PLS1, PLS2, PLS3, and PLS4 multivariate calibration models. Three models are built for the nanostructured Au metasurface. Two exploit the parameters from dips at 46° and 52° separately (PLS1 and PLS2), while the third model (PLS3) combines the parameters of all dips. The fourth model (PLS4) is built for a continuous Au layer. a) Analytical sensitivity  $\gamma$ . b) Root mean square error of prediction RMSEP. c) Resolution  $r_{\text{Sensor}}$ .

the sensitivity of the multivariate calibration model based on the regression coefficients and the uncertainty of the data. The best sensing performance, according to  $\gamma$ , is achieved for the nanostructured Au metasurface when using the combination of the two plasmonic dips and Fresnel reflection features in the MVA model, thus combining the dips  $\approx 46^\circ$  and  $52^\circ$  (PLS3). Compared to the continuous Au layer, we obtain an improvement of a factor of 3.

Furthermore, comparing the metasurface and the continuous layer in terms of  $\gamma$ , but for MVA models based only on the dips  $\approx 52^\circ$  related to SPP effects (thus PLS2 and PLS4, respectively), both models show similar detection performance, with a slightly better result for the continuous Au layer. This outcome is clearly related to a sharper and stronger plasmonic resonance of the continuous layer, as well as smaller fluctuations of the sensor signal in the SPR curves, as shown in Figure 6b. Hence, the RMSEP and  $r_{\text{Sensor}}$  values indicate smaller errors in analyte prediction and lower minimum detectable signal changes for the continuous Au layer. The greater uncertainties found for the localized SPP resonance dip (addressed in PLS2) are also reflected in PLS3, which combines the plasmonic and Fresnel reflection features, where  $r_{\text{Sensor}}$  does not indicate an improvement over the continuous Au layer. Therefore, the enhanced RMSEP for PLS3 of  $\approx 40\%$  (with respect to the continuous Au layer, PLS4) is primarily a result of the highly sensitive and low-noise double dip  $\approx 46^\circ$ , which can be seen in the diagram of Figure 9b; this means that  $r_{\text{Sensor}}$  has also been improved compared to the continuous layer, but only for PLS1 and not for PLS3.

Overall, the combination of plasmonic and Fresnel reflection features strongly enhances the sensing performance using MVA models. The analytical sensitivity improves by 200%, and the prediction errors by 38%. Additionally, the double dip close to the critical angle shows an improved sensing performance compared to the continuous Au layer in terms of the minimum detectable sensor signal for RI changes. The improvement results from an increased number of curve features that are very sensitive to RI changes. Therefore, the performance in data analysis is strongly improved due to more information collected from this double dip. Summarizing,  $\gamma$  is enhanced by 200%, RMSEP by 38%, and  $r_{\text{Sensor}}$  by 23%.

## 4. Conclusion

Our work presents an SPR device consisting of a nanostructured Au metasurface, characterized by several features related to plasmonic resonances, diffraction, and dielectric interface reflections. A multivariate analysis combining all these spectral features enhances the sensing capability of the entire setup. The plasmonic device is excited in Kretschmann configuration and operated at a single wavelength via angular scanning, rendering different plasmonic features. These features stem from the interaction of the LSPR occurring in the Au nanodiscs with the diffraction modes of the array arrangement and from the evanescent field. In addition, characteristic features due to Fresnel reflections at different dielectric interfaces of the whole sensing device, including a microfluidic chamber, help improve sensing performance. In this configuration, the sensor provides high sensitivity to refractive index changes of the analyte and a wealth of features with great potential for enhanced biosensing. Combining the plasmonic and dielectric interface properties of the reflectance curves by multivariate analysis, leads to improved performance in dielectric sensing and results in a 200% improvement in analytical sensitivity and 38% improvement in prediction error compared to a continuous Au layer-based sensor. Considering multiple resonance dips through multivariate analysis improves the sensing performance of current SPR systems and delivers better sensitivity and resolution. The combination of plasmonic and Fresnel features thus opens up new avenues for improved optical environment sensing.

## Supporting Information

Supporting Information is available from the Wiley Online Library or from the author.

## Acknowledgements

This work was supported by the Spanish Ministry of Economy, Industry and Competitiveness under the Maria de Maeztu Units of Excellence Programme – MDM-2016-0618; further financial support by the Basque Government in the Elkartek Programs 2018/19 (KK-2018/00001) and 2020/21

(KK-2020/00001). L.B., N.Z., and J.A. acknowledge financial support from MICIN/AEI/10.13039/501100011033/ under grant PID2022-139579NB-I00 and from the Basque Government under grant no. IT 1526-22 for consolidated groups of the Basque University.

## Conflict of Interest

The authors declare no conflict of interest.

## Data Availability Statement

Research data are not shared.

## Keywords

fresnel reflections, kretschmann configuration, localized surface plasmons, multivariate analysis, partial least squares, plasmonic nanostructures, plasmonic surface lattice resonances

Received: October 20, 2023

Revised: January 29, 2024

Published online:

- [1] P. Singh, *Sens. Actuators, B* **2016**, 229, 110.
- [2] Y. Tang, X. Zeng, J. Liang, *J. Chem. Educ.* **2010**, 87, 742.
- [3] A. M. Shrivastav, U. Cvelbar, I. Abdulhalim, *Commun. Biol.* **2021**, 4, 70.
- [4] J. H. Park, Y. W. Cho, T. H. Kim, *Biosensors* **2022**, 12, 180.
- [5] F. Vollmer, *B.I.F. Futura* **2005**, 20, 239.
- [6] L. Novotny, B. Hecht, *Principles of Nano-Optics*, Cambridge University Press, Cambridge, **2006**.
- [7] A. Kabashin, P. Evans, S. Pastkovsky, W. Hendren, G. A. Wurtz, R. Atkinson, R. Pollard, V. A. Podolskiy, A. V. Zayats, *Nat. Mater.* **2009**, 8, 867.
- [8] G. Armelles, L. Bergamini, A. Cebollada, N. Zabala, J. Aizpurua, *J. Appl. Phys.* **2021**, 129, 073103.
- [9] V. G. Kravets, F. Schedin, R. Jalil, L. Britnell, R. V. Gorbachev, D. Ansell, B. Thackray, K. S. Novoselov, A. K. Geim, A. V. Kabashin, A. N. Grigorenko, *Nat. Mater.* **2013**, 12, 304.
- [10] A. I. Aristov, M. Manousidaki, A. Danilov, K. Terzaki, C. Fotakis, M. Farsari, A. V. Kabashin, *Sci. Rep.* **2016**, 6, 25380.
- [11] S. Zeng, K. V. Sreekanth, J. Shang, T. Yu, C.-K. Chen, F. Yin, D. Baillargeat, P. Coquet, H.-P. Ho, A. V. Kabashin, K.-T. Yong, *Adv. Mater.* **2015**, 27, 6163.
- [12] *Biacore Sensor Surface Handbook*, CY28062 Cytiva, **2022**.
- [13] A. A. Tseng, *Small* **2005**, 1, 594.
- [14] X. D. Hoa, M. Tabrizian, A. G. Kirk, *J. Sens.* **2009**, 2009, 713641.
- [15] N.-H. Kim, W. K. Jung, K. M. Byun, *Appl. Opt.* **2011**, 50, 4982.
- [16] M. Sarkar, M. Besbes, J. Moreau, J.-F. Bryche, A. Olivéro, G. Barbillon, A.-L. Coutrot, B. Bartenlian, M. Canva, *ACS Photonics* **2015**, 2, 237.
- [17] M. Piliarik, P. Kvasnicka, N. Galler, J. R. Krenn, J. Homola, *Opt. Express* **2011**, 19, 9213.
- [18] H.-S. Leong, J. Guo, R. G. Lindquist, Q. H. Liu, *Appl. Phys.* **2009**, 106, 124314.
- [19] A. A. Alwahib, W. H. Muttlak, A. H. Abdulhadi, *Int. J. Nanoelectron. Mater.* **2019**, 12, 145.
- [20] M. Abutoama, I. Abdulhalim, *IEEE J. Sel. Top. Quantum Electron.* **2017**, 23, 72.
- [21] L. Jiang, T. Yin, A. M. Dubrovkin, Z. Dong, Y. Chen, W. Chen, J. K. W. Yang, Z. Shen, *Light Sci. Appl.* **2019**, 8, 21.
- [22] F. Yesilkoy, R. A. Terborg, J. Pello, A. A. Belushkin, Y. Jahani, V. Pruneri, H. Altug, *Light Sci. Appl.* **2018**, 7, 1.
- [23] A. B. Dahlin, N. J. Wittenberg, F. Höök, S.-H. Oh, *Nanophotonics* **2013**, 2, 83.
- [24] J. Etxebarria-Elezgarai, M. Mowat, E. Lopez, C. Rodríguez, I. Olaetxea, A. Seifert, *Anal. Chem.* **2020**, 92, 16236.
- [25] V. G. Kravets, A. V. Kabashin, W. L. Barnes, A. N. Grigorenko, *Chem. Rev.* **2018**, 118, 5912.
- [26] D. I. Yakubovsky, A. V. Arsenin, Y. V. Stebunov, D. Y. Fedyanin, V. S. Volkov, *Opt. Express* **2017**, 25, 25574.
- [27] M. T. Korsa, S. Petersen, N. Rahmani, A. Shabani, Y. K. Mishra, J. Adam, *Nanomaterials* **2022**, 12, 2585.
- [28] P. B. Johnson, R. W. Christy, *Phys. Rev. B* **1974**, 9, 5056.
- [29] D. M. Haaland, E. V. Thomas, *Anal. Chem.* **1988**, 60, 1193.